Frequency-multiplexed terahertz multiple vortex beam generation

Yu Tokizane, Mathias Hedegaard Kristensen, Seigo Ohno, Jérôme Degert, Eric Freysz, Etienne Brasselet, Takeshi Yasui, Emmanuel Abraham

Frequency-multiplexed terahertz multiple vortex beam generation

Yu Tokizane,[1] Mathias Hedegaard Kristensen,[2] Seigo Ohno,[3] Jérôme Degert,[2] Eric Freysz,[2] Etienne Brasselet,[2] Takeshi Yasui,[1] and Emmanuel Abraham[2]

[1)]*Institute of Post-LED Photonics, Tokushima University, 2-1 Minami-Josanjima, Tokushima 770-8506, Japan*

[2)]*CNRS LOMA, UMR 5798, Bordeaux University, Talence, France*

[3)]*Department of Physics, Graduate School of Science, Tohoku University, Sendai 980-8578, Japan*

(*Electronic mail: emmanuel.abraham@u-bordeaux.fr)

(Dated: 26 May 2025)

We propose a simple method to generate a frequency-multiplexed terahertz multiple vortex beam using a spiral phase plate and a metallic mask. Using a broadband terahertz source, we experimentally demonstrate the conversion of a terahertz Gaussian beam into a frequency-multiplexed single or multiple vortex beam with topological charges ranging from 1 to 3, which is supported by simulations. This multifunctional device opens possibilities for high-speed THz communication, information processing, and high-efficiency terahertz wavefront manipulation devices.

An optical vortex beam is characterized by a helical shaped wavefront whose axis is the propagation direction and is associated with a doughnut-shaped intensity profile. This phase is mathematically described by the term $\exp(-i\ell\phi)$, where ϕ represents the azimuthal angle and ℓ is the topological charge. Optical vortices have been widely explored in various fields, including high-speed communications[1,2], high-resolution imaging[3], and optical tweezers that can trap and manipulate microscopic particles due to the orbital angular momentum (OAM) carried by the photons[4,5].

Terahertz (THz) radiation, located between the microwave and infrared regions of the electromagnetic spectrum, has triggered significant interest in recent years. The relatively low energy of THz photons, combined with their ability to penetrate non-conductive materials, make them particularly promising for applications such as security screening, non-destructive imaging, and wireless communications[6–8]. When paired with the unique properties of vortex beams, THz radiation technology holds great potential for the development of advanced high-speed devices capable of handling the growing demand of big data[9]. In recent years, OAM-based mode multiplexing has attracted significant attention in the field of next-generation THz wireless communications. For example, vortex beams multiplexed with different OAM modes can be coupled to a receiver port with a fixed annular index profile, thus increasing the number of communication channels[10–12].

A monomode THz beam can be transformed into multiple beams, each with distinct functionalities such as amplitude, phase, polarization, frequency, and topological charge. This versatility paves the way for the development of innovative devices that harness the full potential of THz vortex beams for next-generation communication systems. Among these devices, multifunctional multichannel metasurfaces have been extensively explored in recent years to generate multiple THz beams with independent control over light properties such as directions, topological charge and frequency[12–17]. These advanced and flexible devices are typically composed of periodic planar arrays of sub-wavelength microstructures with specific phase profiles, enabling the creation of distinct output spatial channels for the incoming radiation[18–24]. Metasurfaces offer significant design flexibility, as they can be tailored to achieve specific properties such as phase and polarization control. However, they are often constrained by specific operating frequencies, which limits their functionality across a broadband spectrum. Although recent work by Yang *et al.* has proposed a dual-band broadband THz OAM device[25], metasurfaces still face challenges such as limited diffraction efficiency of 60 to 70%, which limits the intensity of each channel in a multi-beam system. In addition, OAM purity is often compromised by various factors such as diffraction efficiency, the number of channels, the frequency range, and the topological charge distribution. For multichannel vortex beams, the reported purity levels are usually less than 70%[18,26,27]. These challenges have spurred the search for more efficient, broadband-compatible methods to generate multiple, multifunctional THz vortex beams.

In this letter, we propose a simple and robust method for generating a frequency-multiplexed THz multiple vortex beam using a spiral phase plate, a binary transmission mask, and a broadband THz source. This approach enables the production of a multiple vortex beam with variable topological charges. Our method overcomes the limitations of metasurfaces by enabling broadband operation while maintaining high transmission intensity and achieving decent OAM purity. This opens up possibilities for THz wavefront manipulation, high-speed communication, and information processing applications[22].

In experiments, we used a femtosecond infrared (IR) laser source (800 nm, 1.5 mJ, 50 fs, 1 kHz repetition rate, 5 mm beam waist). The laser output is split into a pump and a probe beam, respectively for THz generation and detection (Fig. 1). Linearly polarized THz pulses, spanning from 0.1 to 2.5 THz, are generated by optical rectification in a $\langle 110 \rangle$-cut ZnTe nonlinear crystal (1 mm thickness, 25 mm clear aperture). After passing through a high-density polyethylene (HDPE) plate, which filters out the remaining pump laser beam, the monomode Gaussian THz beam is converted into a single or multiple vortex beam as follows. The THz beam diameter has been estimated to 7 mm around 1 THz, measured at $1/e^2$ of the maximum beam intensity. In a plane called

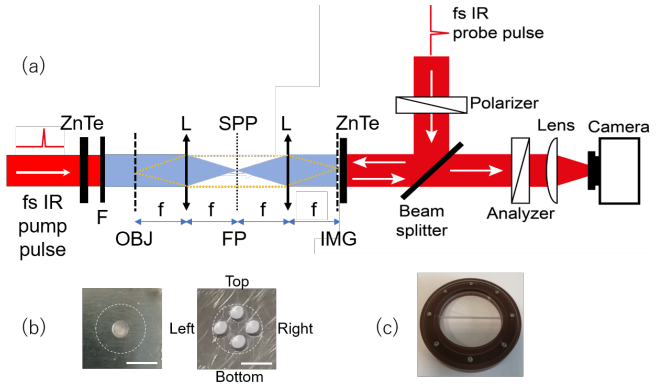

FIG. 1. (a) Experiment. F: HDPE filter, L: TPX THz lens, 50 mm focal length, OBJ: object plane, FP: Fourier plane, SPP: spiral phase plate, IMG: image plane. Red color beam: pump and probe IR laser beams, blue color beam: THz beam, yellow color dashed lines: optical ray tracing between OBJ and IMG planes. (b) Metallic plates with one and four holes. The dotted white circles indicate the size of the THz beam, with a diameter of 7 mm. Scale: white bar is 5 mm. (c) Picture of the Tsurupica SPP.

hereafter the object plane (OBJ), the beam passes through an aluminum mask with one or four drilled circular holes. For the mask with a single hole, the hole diameter is 2.5 mm and the hole is centered on the optical axis. In the four-hole mask, the holes are identical, each with a diameter of 2.5 mm, and centered at each corner of a square with a side length of 3.53 mm. Hole positions are referred to as Top, Bottom, Left and Right (Fig. 1b). Considering the incident 7 mm THz beam diameter, the metallic apertures are properly overfilled by the incident THz radiation, as indicated by the dotted white circles drawn on the metallic masks in Fig. 1b. The mask is then imaged onto another plane, the IMG one, using two identical polymethylpentene (TPX) THz lenses L (50 mm focal length, 38 mm diameter), arranged in a $4f$ imaging configuration. In the IMG plane, the frequency-multiplexed multiple vortex beam will be analyzed. A Tsurupica spiral phase plate (SPP), designed for producing a vortex beam with $\ell = 1$ at 0.43 THz (total step height equals to 1.34 mm), is placed in the focal plane of the first lens (the "Fourier plane", FP) (Fig. 1c). Due to its low dispersion up to few THz, the SPP can generate THz vortex beams with topological charges ℓ at frequencies $\Omega_\ell = 0.43\ell$ THz[28]. Multiple vortex beam generation is achieved by the combined action of the metallic mask and Fourier filtering with the SPP[29,30]. This mechanism introduces also the frequency-multiplexing capability of our device, whose analysis is restricted to $\ell = 1,2$ and 3, which corresponds to $\Omega_1 = 0.43$ THz, $\Omega_2 = 0.86$ THz and $\Omega_3 = 1.29$ THz, respectively.

The spatial profile of the THz vortex electric field is fully reconstructed using a pump–probe detection scheme via the two-dimensional electro-optic sampling (2DEOS) technique[31]. The THz beam is sent onto a second $\langle 110 \rangle$ ZnTe crystal, 1 mm thick with a 25 mm clear aperture, positioned in the IMG plane. Using collinear electro-optic (EO) detection with the time-delayed femtosecond IR probe pulse reflected by the front face (left side) of the crystal, the THz electric field distribution is mapped onto the spatial profile of the IR laser probe beam, which is detected by a CMOS camera[32,33]. The objective lens, located in front of the camera, optically conjugates the ZnTe crystal (THz detector) with the CMOS chip. As EO detection provides both the amplitude and phase of the THz electric field, this experimental setup allows for the reconstruction of the spatial distribution of the THz amplitude and phase in the IMG plane. Specifically, for a given time delay between the THz and the IR probe pulses, the system is able to provide a two-dimensional image, at 800 nm, corresponding to the THz electric field distribution. These images are acquired at a 500 Hz rate, synchronized with the laser repetition rate, and benefit from a dynamic subtraction method[34]. The procedure for measuring the THz electric field has been detailed elsewhere[35]. We typically record $N = 200$ images with a THz-laser probe time delay $\Delta t = 66$ fs between two subsequent images. For each pixel of the camera, the temporal THz waveform can be measured, from which we get the amplitude and phase of the complex THz electric field throughout the 0.1 to 2.5 THz frequency range via the Fourier transform[31,36]. The spectral resolution is given by $1/(N\Delta t) = 0.075$ THz. Additionally, by selecting a spatial region of interest (ROI) within the THz time-domain images, it is also possible to extract the amplitude and phase of the THz electric field at a given frequency within the ROI, providing localized insights into the THz beam.

The first experiment involves converting the THz Gaussian beam into a single vortex beam carrying multiple topological charges ($\ell = 1,2,3$). To achieve this, the metallic mask with a single circular hole is placed in the OBJ plane. Fig. 2 presents the intensity (black and white images) and phase (color images) of the THz beam in the IMG plane at 0.43 THz without the SPP in the FP (($\ell = 0$, row 1), and at 0.43 THz ($\ell = 1$, row 2), 0.86 THz ($\ell = 2$, row 3), and 1.29 THz ($\ell = 3$, row 4) with the SPP in the FP. Columns 1 and 2 correspond to the experimental data, while columns 3 and 4 display the simulations performed using the Python Lightpipes library[37]. This package calculates the propagation, diffraction, and interference of coherent light based on algorithms derived from the scalar theory of diffraction. For the simulations, the characteristics of the THz beam (beam waist, frequency) and the optics (focal lengths, clear optical apertures) were taken into account. Without the SPP in the FP ($\ell = 0$, see Fig. 2, row 1), the geometric image of the object is obtained, with a magnification factor of one. Both experimental and simulation results reflect the intensity distribution (columns 1 and 3) and the uniform phase (columns 2 and 4) of the circular hole. We clearly observe diffraction effects caused by the small size of the hole, which is close to the wavelength of 0.7 mm at 0.43 THz, and clipping of THz radiation by the lenses. As a result, the intensity image of the circular hole (i.e., ℓ = 0) resembles an Airy disk, while the phase experiences π jumps at each oscillation of the electric field. When ℓ is nonzero, the ideal situation (without clipping of the field due to the finite size of the optical elements) leads to an intensity distribution involving gamma and hypergeometric functions[38], which in our case may lead to a number of radial nodes that depends on

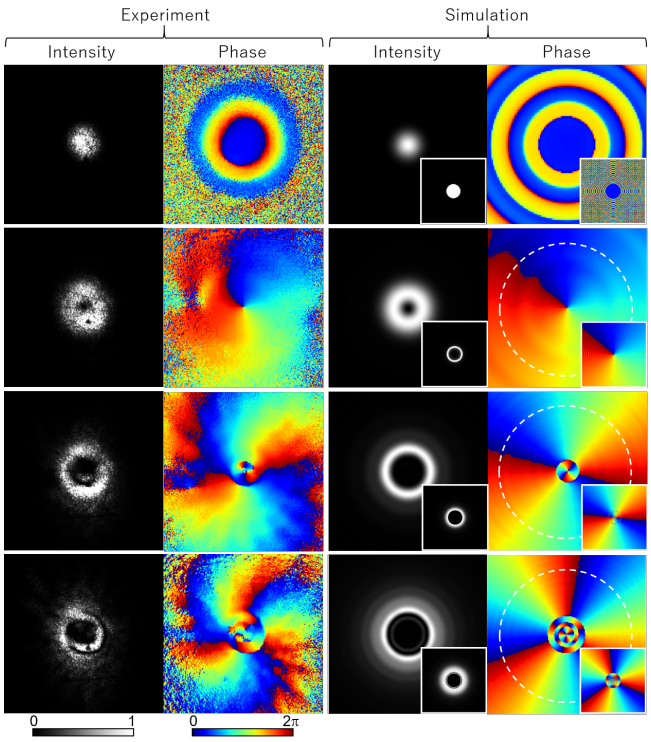

FIG. 2. Frequency-multiplexed THz single vortex beam. First column: experimental intensity, Second column: experimental phase, Third column: theoretical intensity, Fourth column: theoretical phase. Row 1: 0.43 THz, $\ell = 0$. Row 2: 0.43 THz, $\ell = 1$. Row 3: 0.86 THz, $\ell = 2$. Row 4: 1.29 THz, $\ell = 3$. Insets of simulation data: intensity and phase distributions without any diffraction effects . White circles: integration path along the azimuthal angle for global topological charge evaluation. Size of each image: 11×11 mm^2.

ℓ. Insets in simulation data show the intensity and phase considering lenses with infinite radius to remove any diffraction effects. Both the intensity and phase images accurately represent the corresponding intensity and phase distributions of the circular hole. With the SPP, the intensity and phase images at 0.43 THz ($\ell = 1$, row 2), 0.86 THz ($\ell = 2$, row 3), and 1.29 THz ($\ell = 3$, row 4) were calculated. Overall, the simulations support the whole experimental dataset, where π phase jumps in the vicinity of the optical axis are attributed to the oscillations of the electric field (Fig. 2 (rows 3 and 4). In practice, their number and location depend on experimental settings. In addition, we note that the circulation of the phase around a circle enclosing the optical axis and with large enough diameter (see dotted white circles in Fig. 2) equals $2\pi\ell$, which recalls the topological charge ℓ of the used SPP. Again, the insets in the simulation data show the intensity and phase distributions without any diffraction effects. The oscillations of the electric field are much less pronounced resulting in a well-defined central phase singularity.

To examine the quality of the vortex beam, we calculated the OAM purity as follows. The complex amplitude of the THz electric field $A(r,\phi)$ in the spectral domain (at frequency Ω) can be expanded as a sum of the orthogonal vortex modes

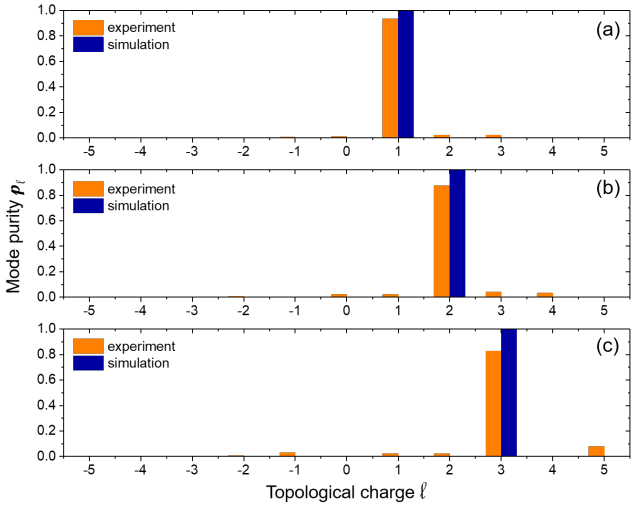

FIG. 3. Frequency-multiplexed THz single vortex beam. Mode purity as a function of topological charge ℓ, from experiment and simulation. Modal decomposition at 0.43 THz (a), 0.86 THz (b), and 1.29 THz (c).

ℓ:

$$A(r,\phi,\Omega) = \sum_{\ell=-\infty}^{+\infty} C_\ell(r,\Omega)\exp(-i\ell\phi), \tag{1}$$

where r is the radial coordinate, and $C_\ell(r,\Omega)$ is the amplitude of the vortex mode characterized by the topological charge ℓ. Using the angular Fourier transformation, we can calculate the decomposition coefficient $C_\ell(r)$ as

$$C_\ell(r,\Omega) = \frac{1}{2\pi}\int_0^{2\pi} A(r,\phi,\Omega)\exp(i\ell\phi)d\phi. \tag{2}$$

The beam power $P_\ell(\Omega)$ carrying the mode ℓ at frequency Ω is then given by

$$P_\ell(\Omega) \propto \int_0^{\infty} |C_\ell(r,\Omega)|^2 2\pi r dr, \tag{3}$$

from which we define the mode purity $p_\ell(\Omega)$ as

$$p_\ell(\Omega) = P_\ell(\Omega) / \sum_{\ell=-\infty}^{+\infty} P_\ell(\Omega). \tag{4}$$

This represents the probability that a photon at frequency Ω is in the ℓ-order OAM state[26]. In our case, we used the experimental amplitude and phase distributions of the THz electric field to compute the $A(r,\phi,\Omega)$ term in Eq. (2), and then calculated the purity of the ℓ mode using Eq. (4). We limited the modal decomposition to span $\ell = \pm 20$ and imposed the normalization condition $\sum_{\ell=-20}^{20} p_\ell(\Omega) = 1$. From simulation (columns 3 and 4, Fig. 2), as expected, the modal decomposition gives $p_\ell(\Omega_\ell = 0.43\ell) = 1$ for $\ell = 1,2,3$ values, as shown in blue in Fig. 3. The experimental modal decomposition, obtained from the data presented in columns 1 and 2 of Fig. 2,

corresponds to the orange bars. The experimental mode purity is in perfect agreement with theory at 0.43 THz, where $p_1(\Omega_1) = 0.93$ (Fig. 3(a)). It is slightly smaller than unity for the other decompositions with $p_2(\Omega_2) = 0.88$ (Fig. 3(b)) and $p_3(\Omega_3) = 0.83$ (Fig. 3(c)), due to the complex and slightly asymmetric intensity and phase distributions of the experimental data shown in Fig. 2 (rows 3 and 4).

Next, we demonstrate the generation of a 2×2 array of THz vortices carrying frequency-multiplexed topological charges $\ell = 1, 2, 3$ by using the four-hole metallic mask. Experimental data for intensity and phase spatial distribution are shown in Fig. 4. Row 1 of Fig. 4 shows the intensity and phase of the THz beam in the IMG plane at 0.43 THz without the SPP ($\ell = 0$) in the FP. It represents the image of the four holes with a uniform phase distorted by diffraction effects, as already discussed. Figure 4 (row 2) shows the situation at 0.43 THz in the presence of the SPP, with excellent agreement between the experimental data and the simulations. Figure 4 (rows 3 and 4)) shows the distribution of THz intensity and phase at 0.86 THz and 1.29 THz in the presence of the SPP in the FP. Although these distributions become complex because of the interaction of multiple vortices, there is still reasonable agreement between experiment and simulation. Again, the evolution of the phase along the white circles in Fig. 4 (rows 2 to 4) confirms the global topological charges of the THz beam with $\ell = 1$ at 0.43 THz, $\ell = 2$ at 0.86 THz, and $\ell = 3$ at 1.29 THz. However, the beam is characterized by a complex vortex with multiple phase singularities. For example, in Fig. 4 (row 2), we observe that the THz beam contains up to nine phase singularities: five with a topological charge of +1 (located at the center of the image and at the center of each hole), characterized by a clockwise phase increase from 0 to 2π, and four with a topological charge of -1, characterized by a counterclockwise phase increase (located between the holes). This configuration maintains the overall topological charge of +1 for the entire THz beam at 0.43 THz. At 0.86 THz (Fig. 4 (row 3)) and 1.29 THz (Fig. 4 (row 4)), the count of all phase singularities is more complex due to high charge splitting and diffraction effects. We also show the intensity and phase distributions obtained after removing the diffraction effects. We observe that, even without diffraction, the topological charge splitting is still severe around the four holes.

From the intensity and phase spatial distributions, we generated a set of four triangular sub-images, referred to as Top, Bottom, Left, and Right, indicated in Fig. 4 (row 2). From these four sub-images, we can calculate the OAM purity. For symmetry reasons, the four modal decompositions from simulation data are identical and presented with the blue bars at 0.43 THz (Fig. 5(a)), 0.86 THz (Fig. 5(b)), and 1.29 THz (Fig. 5(c)). Due to the influence of neighboring holes, the modal spectrum is slightly broadened with peaks at $p_1(0.43\ \text{THz}) = 0.72$, $p_2(0.86\ \text{THz}) = 0.63$, and $p_3(1.29\ \text{THz}) = 0.57$. To mitigate this broadening and tend to the ideal case where $p_\ell(\Omega_\ell = 0.43\ell) = 1$ for all ℓ values, it would be necessary to increase the spacing between the holes and enlarge the THz beam diameter. It is worth mentioning that the decomposition from simulation data without diffraction is similar, indicating that the broadening of the modal

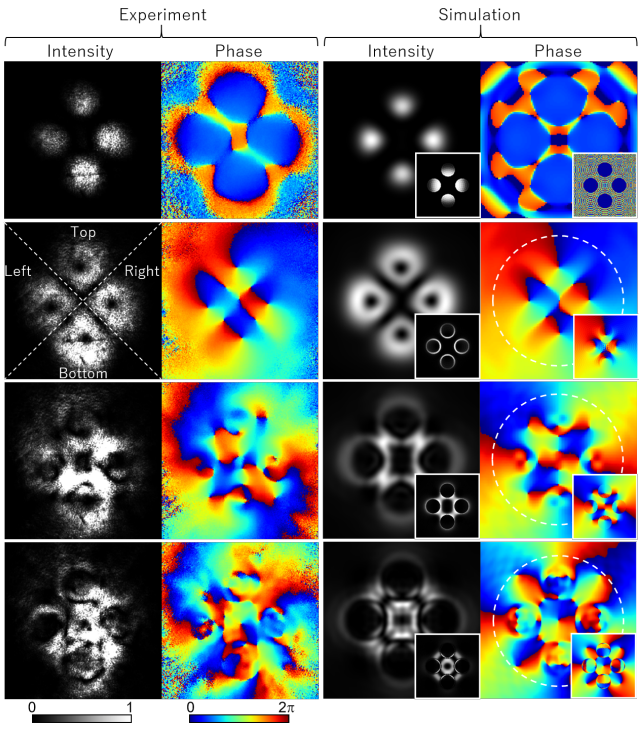

FIG. 4. Frequency-multiplexed THz multiple vortex beam. First column: experimental intensity, Second column: experimental phase, Third column: theoretical intensity, Fourth column: theoretical phase. Row 1: 0.43 THz, $\ell = 0$. Row 2: 0.43 THz, $\ell = 1$. Row 3: 0.86 THz, $\ell = 2$. Row 4: 1.29 THz, $\ell = 3$. Insets on simulation data: intensity and phase distributions without any diffraction effects. White circles: integration path along the azimuthal angle for global topological charge evaluation. Size of each image: 11×11 mm^2.

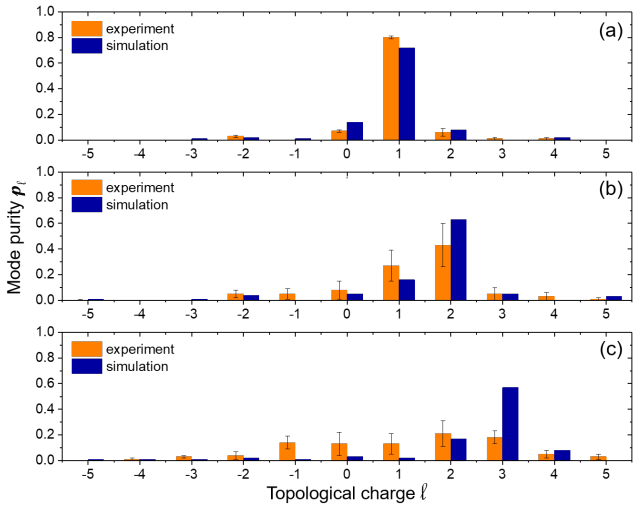

FIG. 5. Frequency-multiplexed THz multiple vortex beam. Mode purity as a function of topological charge ℓ, from experiment (averaging of four holes) and simulation. Modal decomposition at 0.43 THz (a), 0.86 THz (b), and 1.29 THz (c).

decomposition is mainly due to the presence of multiple holes in the object plane instead of lens clipping. For the experiment, the modal decomposition is slightly different as a function of hole position, due to THz beam inhomogeneity, optical misalignment, geometric aberrations induced by optical components, and imperfect mask design. Consequently, we calculated, and plotted with orange bars in Fig. 5 the average modal decomposition of the four sub-images. The experimental mode purity is 0.8 at 0.43 THz ($\ell = 1$), close to the theoretical value of 0.72. The mode purity decreases to 0.43 ± 0.17 at 0.86 THz ($\ell = 2$), with large error bars resulting from beam inhomogeneities. At 1.29 THz ($\ell = 3$), the mode purity is not better than 0.2 for both $\ell = 2$ and 3. This degradation is again attributed to the high charge splitting and diffraction effects.

As a discussion, if we consider a broadband THz source and detection, we can extend our demonstration to higher frequencies and larger topological charges. For example, considering a 0.1 to 10 THz emission and detection associated with a non-dispersive SPP designed for $\ell = 1$ at 0.43 THz, we could generate a frequency-multiplexed THz vortex beam across up to 23 independent frequencies, such as 0.43, 0.86, ..., 9.89 THz. This represents a unique characteristic compared to metasurface devices, which are usually designed for a single frequency. Additionally, by flipping the SPP, negative values of the topological charges can be directly obtained. However, positive or negative values of the topological charges can be addressed, but not both simultaneously. Finally, from a more general perspective, our device could be used for the optical transmission of information, with addressable amplitude, phase, frequency, topological charge, and polarization for each vortex. For example, the modulation of amplitude and polarization could be adjusted by controlling the transmission of THz radiation through each individual hole drilled in the metallic plate by means of neutral densities, polarizers or appropriate waveplates. This could pave the way for the development of versatile platforms for encoding and manipulating data in future high-speed THz communication systems.

In conclusion, we have proposed an approach for generating frequency-multiplexed THz multiple vortex beams. Rather than relying on specifically designed metasurface devices, we used a binary metallic mask and a SPP placed in the FP of a lens. Coupled with a broadband THz source, we were able to generate single and multiple vortex beams, multiplexed in frequency with topological charges ranging from 1 to 3. This innovative approach could inspire the THz community to explore applications in material patterning and structuration, THz wavefront beam shaping, and the development of high-speed devices dedicated to big data manipulation.

This work was supported by the department Sciences de la Matière et du Rayonnement (Bordeaux University).

AUTHOR DECLARATIONS

Conflict of interest

The authors have no conflicts to disclose.

Author contributions

All the authors contributed equally to this work.

DATA AVAILABILITY

The data that support the findings of this study are available from the corresponding author upon reasonable request.

REFERENCES

[1]J. Wang, J.-Y. Yang, I. Fazal, N. Ahmed, Y. Yan, H. Huang, Y. Ren, Y. Yue, S. Dolinar, M. Tur, and A. E. Willner, "Terabit free-space data transmission employing orbital angular momentum multiplexing," Nature Photonics **6**, 488 – 496 (2012).

[2]N. Bozinovic, Y. Yue, Y. Ren, M. Tur, P. Kristensen, H. Huang, A. E. Willner, and S. Ramachandran, "Terabit-scale orbital angular momentum mode division multiplexing in fibers," Science **340**, 1545–1548 (2013).

[3]Y. Shen, X. Wang, Z. Xie, C. Min, X. Fu, Q. Liu, M. Gong, and X. Yuan, "Optical vortices 30 years on: OAM manipulation from topological charge to multiple singularities," Light: Science Applications **8**, 90 (2019).

[4]H. He, M. E. J. Friese, N. R. Heckenberg, and H. Rubinsztein-Dunlop, "Direct observation of transfer of angular momentum to absorptive particles from a laser beam with a phase singularity," Phys. Rev. Lett. **75**, 826–829 (1995).

[5]D. Grier, "A revolution in optical manipulation," Nature **424**, 810–816 (2003).

[6]M. Perenzoni and D. J. Paul, *Physics and Applications of Terahertz Radiation*, 1st ed., Springer Series in Optical Sciences (Springer Netherlands, Dordrecht, 2014).

[7]T. Kürner, D. Mittleman, and T. Nagatsuma, *THz Communications: Paving the Way Towards Wireless Tbps*, Springer Series in Optical Sciences (Springer International Publishing, 2021).

[8]T. Nagatsuma, G. Ducournau, and C. Renaud, "Advances in terahertz communications accelerated by photonics," Nature Photonics **10**, 371–379 (2016).

[9]X. Wang, Z. Nie, Y. Liang, J. Wang, T. Li, and B. Jia, "Recent advances on optical vortex generation," Nanophotonics **7**, 1533–1556 (2018).

[10]Y. Yang, Z. Yang, and J. Liu, "Terahertz quasi-perfect vortex beams," Infrared Physics Technology **136**, 104870 (2024).

[11]W. Shao, S. Huang, X. Liu, and M. Chen, "Free-space optical communication with perfect optical vortex beams multiplexing," Optics Communications **427**, 545–550 (2018).

[12]K. Guo, M. Zhang, Z. Du, and Z. Song, "Terahertz spin-selective metasurface for multichannel switching of OAM," Results in Physics **56**, 107279 (2024).

[13]X. Li, W. Wei, and X. Yang, "Multi-functional terahertz metasurface for a vortex beam, multi-channel focusing, polarization conversion, and broadband absorption based on vanadium dioxide," Appl. Opt. **63**, 1695 (2024).

[14]J. Liang and M. Dai, "Optically reconfigurable multi-channel orbital angular momentum generator based on 3-bit coding metasurface," AIP Advances **14**, 075022 (2024).

[15]Z. Ren, Y. Zhao, W. Wang, H. Yao, G. Ren, S. Li, and R. Wang, "Polarization and frequency multiplexed multi-channel focusing terahertz vortex with a birefringent dielectric metasurface," Phys. Scr. **99**, 065508 (2024).

[16] J. Zhan, R. Nie, R. Zhang, C. Tang, F. Zhao, Z. Chen, S. Huang, S. Cao, J.-h. Chen, and Z. Song, "Achieving broadband multifunctional modulation of wavefront via terahertz anisotropic metasurface," Results in Physics **64**, 107930 (2024).

[17] H. Zhang, X. Sang, Z. Li, K. Wang, X. Lv, C. Jiang, X. Sun, L. Meng, and Y. Zhang, "Bidirectional multi-mode multiple vortex beams generator based on terahertz metasurface," Optics Communications **558**, 130371 (2024).

[18] D. Zhang, Z. Lin, J. Liu, J. Zhang, Z. Zhang, Z.-C. Hao, and X. Wang, "Broadband high-efficiency multiple vortex beams generated by an interleaved geometric-phase multifunctional metasurface," Opt. Mater. Express **10**, 1531 (2020).

[19] W. Liu, Q. Yang, Q. Xu, X. Jiang, T. Wu, J. Gu, J. Han, and W. Zhang, "Multichannel terahertz quasi-perfect vortex beams generation enabled by multifunctional metasurfaces," Nanophotonics **11**, 3631–3640 (2022).

[20] J.-S. Li and Y. Chen , "Multi-channel terahertz focused beam generator based on shared-aperture metasurface," Chinese Phys. B **32**, 124204 (2023).

[21] J.-s. Li, F.-l. Guo, and Y. Chen, "Multi-channel and multi-function terahertz metasurface," Optics Communications **537**, 129428 (2023).

[22] W. Guan, Y. Qi, H. Li, X. Ding, Y. Tan, and X. Wang, "Reconfigurable metasurface with multi-vortex beam regulation and shared aperture focusing," J. Opt. Soc. Am. B **41**, 2425 (2024).

[23] P. Gao, C. Chen, Y. Dai, X. Wang, H. Cui, X. Zhu, and H. Liu, "Reconfigurable janus metasurface with chiral meta-atoms for multi-channel vortex beams and holography multiplexing," Opt. Express **33**, 309–321 (2025).

[24] Y. Xiao and K. Liao, "Multipolar multifunction terahertz tunable metasurface," Appl. Opt. **64**, 874 (2025).

[25] Y. Yang, X. Wang, J. Zhang, G.-M. Yang, and N. Chi, "Dual-band broadband terahertz orbital angular momentum metasurface," Opt. Express **32**, 46004 (2024).

[26] Z. Zhou, Y. Qi, B. Zhang, Y. Wen, L. Wang, and X. Wang, "Dual-mode switchable metasurface for multi-type OAM vortex beam generation and dual-band perfect absorption in terahertz band," Phys. Scr. **98**, 105518 (2023).

[27] J.-S. Li, M.-Y. Jiang, and R.-H. Xiong, "Bidirectional vortex beam and reflective polarization conversion terahertz metasurfaces," Appl. Opt. **63**, 4637 (2024).

[28] K. Miyamoto, K. Suizu, T. Akiba, and T. Omatsu, "Direct observation of the topological charge of a terahertz vortex beam generated by a tsurupica spiral phase plate," Applied Physics Letters **104**, 261104 (2014).

[29] S. Fürhapter, A. Jesacher, S. Bernet, and M. Ritsch-Marte, "Spiral phase contrast imaging in microscopy," Opt. Express **13**, 689 (2005).

[30] M. Ritsch-Marte, "Orbital angular momentum light in microscopy," Phil. Trans. R. Soc. A. **375**, 20150437 (2017).

[31] A. Minasyan, C. Trovato, J. Degert, E. Freysz, E. Brasselet, and E. Abraham, "Geometric phase shaping of terahertz vortex beams," Opt. Lett. **42**, 41 (2017).

[32] Q. Wu, W. Fan, and C. Qin, "Generation and Superposition of Perfect Vortex Beams in Terahertz Region via Single-Layer All-Dielectric Metasurface," Nanomaterials **12**, 3010 (2022).

[33] G. Gallot and D. R. Grischkowsky, "Electro-optic detection of terahertz radiation," Journal of The Optical Society of America B-optical Physics **16**, 1204–1212 (1999).

[34] Z. Jiang, X. G. Xu, and X.-C. Zhang, "Improvement of terahertz imaging with a dynamic subtraction technique," Appl. Opt. **39**, 2982–2987 (2000).

[35] M. Brossard, H. Cahyadi, M. Perrin, J. Degert, E. Freysz, T. Yasui, and E. Abraham, "Direct Wavefront Measurement of Terahertz Pulses Using Two-Dimensional Electro-Optic Imaging," IEEE Transactions on Terahertz Science and Technology **7**, 741–746 (2017).

[36] A. A. Dhaybi, J. Degert, E. Brasselet, E. Abraham, and E. Freysz, "Terahertz vortex beam generation by infrared vector beam rectification," Journal of the Optical Society of America B **36**, 12 (2019).

[37] "Lightpipes for python," https://opticspy.github.io/lightpipes/.

[38] Carlotti, A., Ricort, G., and Aime, C., "Phase mask coronagraphy using a mach-zehnder interferometer," AA **504**, 663–671 (2009).